Dynamics of Fe adsorption and desorption from CoO_xH_y during oxygen evolution reaction electrocatalysis

Lu Liu[1,3,5], Liam P. Twight[1], Shibo Xi[5], Yingqing Ou[1,4*] and Shannon W. Boettcher[1,2*]

[1] Department of Chemistry and Biochemistry and the Oregon Center for Electrochemistry, University of Oregon, Eugene, Oregon 97403, United States

[2] Department of Chemical & Biomolecular Engineering and Department of Chemistry, University of California, Berkeley, and Energy Storage and Distributed Resources Division, Lawrence Berkeley National Laboratory, Berkeley, CA 94720, United States

[3] School of Materials Science and Engineering, Chongqing University, Chongqing 400044, China

[4] School of Chemistry and Chemical Engineering, Chongqing University, Chongqing 400044, China

[5] Institute of Sustainability for Chemicals, Energy and Environment (ISCE2), Agency for Science, Technology and Research (A*STAR), 1 Pesek Road Jurong Island, Singapore, 627833, Singapore

AUTHOR INFORMATION

Corresponding Author

*Shannon W. Boettcher: boettcher@berkeley.edu

*Yingqing Ou: yingqing@uoregon.edu

Notes

The authors declare no competing financial interest.

Abstract

Iron plays a central and critical role in the water oxidation mechanism and activity of transition-metal oxides and (oxy)hydroxides. Tracking Fe dynamics (deposition/dissolution/electrolyte-transport) and unravelling the chemistries of various Fe active-sites under oxygen-evolution-reaction (OER) conditions are important for catalyst design, particularly for applications in alkaline electrolysis. Here we use CoO_xH_y thin films as a platform to investigate Fe transport and reactivity at the catalyst-electrolyte interface and its impact on OER activity. We find that the deposition/dissolution of the surface-absorbed Fe species are governed by soluble Fe species transport and applied potential. Soluble Fe species in the electrolyte adsorb on CoO_xH_y under stirred electrolyte conditions. Accelerated Fe desorption is observed with more-positive OER potential. The surface-localized Fe sites generated by absorption from soluble Fe species have a higher OER turnover frequency (TOF_{Fe}) compared to Fe in co-deposited $CoFeO_xH_y$ films. *Operando* X-ray absorption spectroscopy shows structural similarity between reference Fe oxyhydroxides and surface Fe sites on CoO_xH_y, contrasting with Fe sites within the CoO_xH_y structure made by co-deposition where Fe shows a different apparent x-ray absorption edge energy. The OER activity of the surface-absorbed Fe decreased by Fe desorption but was recoverable by re-depositing Fe species under non-OER conditions.

Keywords: oxygen evolution reaction, $CoFeO_xH_y$, Fe-spike experimental, Fe adsorption and desorption

1 Introduction

Water electrolysis from renewable electricity generates green H_2, a fossil-fuel-free energy carrier well-suited for long-duration energy storage and heavy industry.[1-5] The efficiency of water electrolysis faces challenges, particularly from the oxygen evolution reaction (OER), where large overpotentials are required to drive the slow four-electron-transfer reaction.[6-9] Previous research has focused on earth-abundant Ni and Co based catalysts. Under alkaline conditions, the structural reconstruction of precursor materials results in the formation of surface (oxy)hydroxides, which have been recognized as the active phase towards OER.[10-15] Notably, the leading catalytic activity of Co and Ni (oxy)hydroxide is observed only upon the incorporation of Fe, resulting in an increase in activity by up to 30 and 1000-fold, respectively.[16, 17]

Despite a substantial body of research dedicated to the role of Fe in Fe-doped Ni and Co-based systems, the mechanism through which Fe enhances activity is not fully elucidated. Friebel et al. combined *operando* X-ray absorption spectroscopy (XAS) with DFT calculations, which identified Fe-centered motifs as the active site in $Ni_{1-x}Fe_xOOH$. It was proposed that the shorter Fe-O bond length compared with γ-FeOOH led to optimized adsorption of intermediates during OER and lowered overpotential.[18] For the $Co(Fe)O_xH_y$ system, *in-situ XAS* showed partial Fe oxidation and the shortening of Fe-O bond distance during OER-relevant potentials, while the Co oxidation state was unchanged.[19] As charge transfer is required for OER, this result suggested that the active site changed from Co- to Fe-centered upon Fe incorporation. Chen et al. observed Fe^{4+} species during steady-state OER by using operando Mössbauer spectroscopy, but that these Fe^{4+} species were purportedly not kinetically competent.[20] In contrast, other work showed that the OER activity of mixed Co-Fe oxides mirrored the population of Fe^{4+} detected, suggesting a prominent role of Fe in promoting the OER.[21]

An important aspect of the overall microscopic picture of OER catalysis by Fe-based sites is how they maintain high OER activity over extended periods via an apparent dissolution-redeposition mechanism. This mechanism appears driven by the thermodynamic instability of FeOOH under oxidative and alkaline conditions.[22, 23] Chung *et al.* showed that a Fe dissolution and redeposition steady-state was established when a small amount of soluble Fe species was in the electrolyte.[24] A recent work visualized the Fe incorporation process from the electrolyte into

the NiO host material.[25] Initial voltammetry cycles revealed the presence of a superficial NiFe LDH layer, contributing to a reduction in OER overpotential. However, activity loss was observed in a subsequent constant-potential electrolysis step associated with the formation of aggregated FeO_x.

We have previously argued that the way Fe interacts with the host materials is related to the electrochemical history and the intrinsic structural properties of the host metal (oxy)hydroxides.[17, 26] When CoO_xH_y was tested in Fe-spiked KOH, the incorporated Fe species, whether via constant-potential electrolysis or voltametric cycling, did not substantially change the redox-peak profiles of nominal $Co(OH)_2$/CoOOH couple, which suggests that the Fe is only adsorbed on the surface region of CoO_xH_y.[27] Differently, upon cycling in Fe-spiked KOH, the Fe cations apparently mix with the Ni species, as evidenced by the positive shift of the $Ni(OH)_2$/NiOOH redox peaks, while under constant-potential electrolysis the Fe was confined to the surface of NiO_xH_y. Thus, compared to the more-dynamic $Ni(Fe)O_xH_y$ system, $Co(Fe)O_xH_y$ provides a useful platform where mixing between surface-adsorbed and internal (less-active) Fe-based sites is suppressed.[26] This enables investigating how operational parameters, such as electrochemical methods and Fe-species electrolyte transport to the solid-liquid interface affect the adsorption-desorption of reactive Fe sites and subsequent OER performance.

Here, we report on the dynamics of Fe at the CoO_xH_y-electrolyte interface. Our findings show that the steady-state Fe concentration at the catalyst surface results from the combined influence of electrolyte transport and applied potential. Through experiments with and without mechanical stirring, we identified that Fe adsorption is in part governed by its transport in the electrolyte. Furthermore, we observed an acceleration in Fe dissolution with elevated positive potential, particularly in regions relevant to the OER. Next, we quantitatively compared the OER activity of two putative Fe sites: surface Fe sites prepared through voltammetry cycling in Fe^{3+} spiked KOH and predominantly bulk Fe sites in co-electrodeposited CoFe (oxy)hydroxides. The structural disparities contributing to the differing OER activities of surface and bulk Fe sites were then analyzed with *operando* XAS. Finally, the catalytic stability of $Co(Fe)O_xH_y$ was studied. A decrease in OER activity due to Fe leaching could be reversed by implementing short chronoamperometry (CA) interruptions over a potential range where OER does not occur. This

approach provides a viable strategy to mitigate activity degradation during long-term water electrolysis or variable-load alkaline water electrolysis driven by renewable electricity.

2 Experimental

2.1 Reagents and Materials

Cobalt nitrate hexahydrates ($Co(NO_3)_2 \cdot 6H_2O$, 99.999% trace metal basis, Sigma Aldrich), iron nitrate hexahydrates ($Fe(NO_3)_3 \cdot 6H_2O$, 99.99% metal basis, Sigma Aldrich) and ferrous chloride ($FeCl_2 \cdot 6H_2O$, 98%, Sigma Aldrich) were used as received. Potassium hydroxide (semiconductor grade, 99.99%, Sigma Aldrich) was used as received or was purified (Section 2.3). All solutions were prepared with deionized (DI) 18.2 MΩ·cm water. All solutions were transferred into an acid-cleaned polypropylene bottle for storage before use.

2.2 Solution and metal hydroxide film preparation

For electrochemical characterization, catalyst films were deposited on Pt (50 nm)/Ti (50 nm) metal layers deposited on glass-slide substrates. The procedure for preparing the Pt electrodes is described in previous work.[28] CoO_xH_y films were electrodeposited from an aqueous solution of 0.1 M $Co(NO_3)_2 \cdot 6H_2O$. To prepare the co-deposited $CoFeO_xH_y$ films, $FeCl_2 \cdot 6H_2O$ was introduced into the deposition solution in varying ratios of Co and Fe, while maintaining a total metal ion concentration of 0.1 M. Before adding $FeCl_2 \cdot 6H_2O$, the electrodeposition solution was sparged with N_2 for at least 20 min to minimize the oxidation of Fe^{2+} to Fe^{3+}. Cathodic electrodeposition was carried out using a two-electrode setup system at a current density of -2 mA/cm^2 for a duration of 8 s, unless specified otherwise (driving nitrate reduction and causing a local pH increase, and thus precipitating the solid (oxy)hydroxide at the electrode surface). After electrodeposition, the working electrode was promptly removed from the solution and rinsed with water to prevent the dissolution of the freshly deposited hydroxides in the acidic deposition solution.

For the XAS measurements, carbon paper was used as a substrate for depositing $Co(Fe)O_xH_y$. Prior to electrodeposition, the carbon paper was refluxed in concentrated aq. HNO_3 (70%) for 6 h to remove impurities and enhance the hydrophilicity. Following reflux, the carbon

paper was rinsed with deionized (DI) water and absolute ethanol multiple times, then dried at 60 ^{o}C. CoO_xH_y was electrodeposited onto the carbon paper using a 0.1 M $Co(NO_3)_2{\cdot}6H_2O$ aqueous solution. $Co_{0.8}Fe_{0.2}O_xH_y$ was deposited by using a mixture of 0.1 M $Co(NO_3)_2{\cdot}6H_2O$ and $FeCl_2{\cdot}6H_2O$ solution, with a Co/Fe molar ratio of 4:1. The deposition process involved applying a constant current density of -2 mA/cm^2 for 8 s. This deposition cycle was repeated four times, with an interval time of 8 s between each cycle.

2.3 Fe, Co-free Electrolyte preparation

Freshly prepared $Co(OH)_2$ precipitates were used as the absorbent to remove Fe impurities in semiconductor grade KOH solution. The detailed procedures can be found in previous work.[16, 17] Residual Co species in Fe-free electrolyte were purified by 0.1 μm filter (hydrophilic Acrodisc polyethersulfone) and the purified KOH solution was stored in an acid-cleaned polypropylene bottle.[29]

2.4 Fe-spiking procedures

For all Fe-spiking experiments, unless stated otherwise, the Fe concentration in the KOH electrolyte was maintained at 0.1 ppm. To achieve this, a stock solution was prepared by dissolving $Fe(NO_3)_3{\cdot}9H_2O$ in DI water, resulting in a Fe^{3+} concentration of 0.1 mM. To prevent Fe^{3+} hydrolysis and precipitation, the pH value of the stock solution was adjusted to ~1.0 by adding concentrated HNO_3 solution (68-70%). The successful inhibition of Fe^{3+} hydrolysis was indicated by the nearly colorless appearance of the stock solution (as opposed to a yellow coloration). Typically, after the preparation of the CoO_xH_y film, it was initially subjected to 2-4 voltammetry cycles or chronoamperometry tests to achieve a stable electrochemical response. Subsequently, a specific volume of the 0.1 mM Fe^{3+} stock solution was added to the KOH electrolyte, resulting in a Fe concentration of 0.1 ppm. The amount of Fe^{3+} stock solution added depended on the volume of KOH electrolyte used for the electrochemical tests.

2.5 Electrochemical measurements

All electrochemical measurements were conducted with a BioLogic SP300 or SP200 potentiostat with a three-electrode setup. A Pt coil cleaned with aqua regia was used as the counter electrode. The reference electrode was Hg/HgO (CH Instruments, CHI 152) filled with 1 M KOH, which was

regularly calibrated against a reversible hydrogen electrode to ensure accuracy. To prevent contamination, separate Hg/HgO reference electrodes were used for "Fe-free" and Fe-containing electrochemical measurements, respectively. The electrochemical cells were made with polypropylene (Nalgene) and were thoroughly cleaned with 1 M H_2SO_4 and DI water before each use. The glass section of the working electrode was covered with hot glue.

During cyclic voltammetry and chronoamperometry measurements, real-time iR_u compensation was not applied. Instead, manual iR_u compensation was used if needed after the electrochemical tests. The value of R_u was determined by equating it to the minimum impedance within the frequency range of 10 kHz to 1 MHz, where the phase angle approached zero. In 1 M KOH electrolyte, the recorded potential versus Hg/HgO was converted to the reversible hydrogen electrode (RHE) scale using the equation $E_{RHE} = E_{Hg/HgO} + 0.924$ V. The overpotential (η) was calculated based on the equation $\eta = E_{RHE} - 1.23$ V.

2.6 Materials characterization

X-ray photoelectron spectroscopy (XPS, ESCALAB 250, Thermo Scientific) data were collected and used to study the surface composition of the metal hydroxide films and the ratio determined in the Co/Fe. An Al Kα non-monochromated flood source was used to collect cobalt spectra and an Mg Kα non-monochromated flood source for Fe. Scanning electron micrograph (SEM, Zeiss Ultra 55 SEM) images were analyzed to understand morphology changes**.** The *operando* X-ray absorption fine structure (XAS) data were collected at the XAFCA beamline of the Singapore Synchrotron Light Source (SSLS) under fluorescence mode. The storage ring of SSLS was running at 0.7 GeV with an electron current of 200 mA. Energy calibrations were carried out using standard Co and Fe foils. The *operando* XAS data was collected under ambient conditions in the electrochemical cell as shown in Figure S6, while a constant potential was applied to the working electrode. Hg/HgO served as reference electrode and Pt coil as the counter electrode. Athena software was used for energy calibration and background removal.

2.7 In situ mass changes

An electrochemical quartz-crystal microbalance (EQCM, Stanford Research Systems QCM200) electrode was used to monitor the in-situ mass changes of films during electrochemical measurements. Films were deposited on 5 MHz AT-cut Pt/Ti quartz crystals. The film

electrodeposition on the EQCM electrode was identical to that on Pt/Ti substrates. The collected EQCM frequency change was converted to mass change based on the Sauerbrey equation:

$$\Delta f = -C_f \cdot \Delta m$$

Where Δf is the experimental frequency change, C_f (56.6 Hz cm^2 g^{-1}) is the sensitivity factor and Δm is the mass change per geometric area of the QCM electrode (1.38 cm^2).[16] EQCM electrodes were cleaned in 1 M H_2SO_4 by cycling from -2.0 V to 2.0 V for 2 cycles and then cycled in 1 M Fe-free KOH to ensure the substrate is free of Ni or Co contamination whose presence is indicated by the appearance of redox features in the pre-OER potential range.

2.8 Turnover Frequency (TOF) calculation

TOF values were calculated from the cyclic voltammetry measurements. To compare the intrinsic activity of different types of Fe species, TOF_{Fe} based on the mass of Fe in the catalyst film was calculated from:

$$TOF_{Fe} = \frac{i / 4F}{(\text{mol of Fe sites})}$$

Where *i* refers to the average OER current of the forward and reverse sweep at an overpotential of 325 mV (iR_u compensated), *F* is the Faraday constant (96485 C/mol). The Fe mass was determined by ICP-MS (the details are in Section 2.9).

2.9 Elemental analysis

To quantify the mass of Fe and Co in the catalyst film, the working electrodes were immersed in a 5% vol. HNO_3 solution (trace-metal grade, Fischer Scientific) of 4 mL for at least 24 h. After removing the electrodes from the HNO_3 solution, they were rinsed with DI water. Subsequently, cyclic voltammetry tests were conducted in 1 M KOH. The absence of Co redox peaks and a similar electrochemical response to the bare Pt/Ti substrate indicated complete dissolution of the catalyst films. The 5% vol. HNO_3 solution containing the dissolved metal ions was used for analysis by inductively coupled plasma mass spectrometry (ICP-MS, iCAP-RQ Qnova from Thermo Fisher Scientific). During data acquisition, counts for each element were analyzed three times, and the average value was reported. Each type of catalyst was prepared and analyzed by ICP-MS analysis at least three times. The error bars were plotted based on the results of the parallel analyses. Concentrations are reported as an average ± one standard deviation. All calibration curves were

generated using third-party-certified reference solutions of the respective analytes of interest, such as Cobalt and Iron ICP-MS standards (10 ± 1 ppm, Ricca), Yttrium standard solution (1001 ± 4 ppm, Aristar), and Scandium standard (994 ± 6 ppm, Sigma Aldrich).

3 Results and discussion

3.1 Electrochemical properties of CoO_xH_y in Fe-free condition

CoO_xH_y films were prepared by cathodic electrodeposition using Pt/Ti/glass as the substrate, as Pt has negligible OER activity even in Fe-containing electrolyte. The mass loading of CoO_xH_y is 16 ± 1 μg cm^{-2}, as determined ICP-MS analysis (see experimental section). The CoO_xH_y films exhibit a typical porous nanosheet structure as revealed by the SEM image (inset of Figure S1a).[30] The porous structure is beneficial for the exposure of catalyst to the electrolyte and provides an useful platform for the study of Fe ion adsorption-desorption at the catalyst-electrolyte interface.

The voltametric analysis of CoO_xH_y revealed a pair of redox waves at 0.15-0.2 V vs. Hg/HgO. These redox peaks correspond to the electrochemical conversion between nominal Co^{2+} and Co^{3+} species.[30] The amount of charge transferred during this redox process can be calculated by integrating the areas under the cathodic and anodic peaks. In the first voltammetry cycle of CoO_xH_y, the integrated charge of the anodic peak in the forward scan was larger than that of the cathodic peak in the backward scan. Subsequent second and third cycles showed no significant change in peak area. This irreversible oxidation behavior is pronounced in Co systems and can be (in part) attributed to differences in conductivity between CoOOH and $Co(OH)_2$.[31, 32] When the more-conductive CoOOH is reduced, an insulating $Co(OH)_2$ layer forms near the metal-substrate/current-collector region. This insulating layer probably impedes electron transfer and prevents further reduction of the outer portion of CoOOH.[16, 33]

To address this limitation, we prepared thinner CoO_xH_y films by passing less charge during the electrodeposition process (−0.2 mA/cm^2 for 25 s, resulting in 5 mC passed), hypothesizing that this approach would mitigate or eliminate the asymmetry observed in the first cycle. As shown in Figure S1b, the anodic peak in the first cycle exhibited a similar integrated area to that of the corresponding cathodic peak and the subsequent redox peaks. This suggests that the outer CoOOH layer is no longer “trapped” in the thinner film, which can be attributed to the reduced distance electrons must transport to drive the complete redox of the catalyst film.

3.2 Fe adsorption-desorption dynamics at the catalyst-electrolyte interface

Our previous studies demonstrated that soluble Fe species in the KOH electrolyte can be adsorbed onto accessible sites of Ni and Co (oxy)hydroxides, thereby enhancing their oxygen evolution reaction (OER) activity.[16, 34] Investigating the dynamics of Fe adsorption-desorption at the catalyst-electrolyte interface and how these anchored Fe sites catalyze the OER is useful for developing a comprehensive understanding of the reaction mechanism(s) and designing higher performance practical catalyst systems across alkaline-electrolysis technologies. We note that we refer to Fe sites in this study because the presence of Fe is a requirement for higher OER activity, but recognize that the assignment of the precise structure of the active site is not possible and the active site chemistry almost certainly involves contributions from both Fe and Co cations.[16, 26, 28]

To address this knowledge gap, we propose a simple chemical equilibrium to describe the Fe adsorption-desorption process: $Fe^{3+}(aq) + * \rightarrow Fe(ads)$, where * presents the accessible site on CoO_xH_y for Fe adsorption. Assuming that CoO_xH_y is exposed to the same external conditions, such as temperature and applied potential, the number or density of accessible sites and the equilibrium constant is assumed constant. Consequently, the quantity of $Fe_{(ads)}$ is directly influenced by the concentration of $Fe^{3+}(aq)$ near the CoO_xH_y surface. As the solubility of $Fe^{3+}(aq)$ in 1 M KOH is low, transport of $Fe^{3+}(aq)$ to the surface is also likely important.

To assess this simple picture, we varied the Fe-ion transport by controlling stirring of the electrolyte while the Fe adsorption was monitored via changes in the OER activity. Figure 1a-e shows the OER activity of CoO_xH_y as a function of voltametric cycle number in Fe-free and Fe-spiked KOH under various stirring conditions. CoO_xH_y in rigorously Fe-free electrolyte exhibits low OER activity (Figure S2a). In Fe-containing measurements, Fe^{3+} (0.1 ppm) was first added into the electrolyte and stirred to ensure its even distribution. During the first 1-4 voltammetry cycles without mechanical stirring, the OER current at 0.7 V vs. Hg/HgO was stable (Figure 1a) and close to that in Fe-free condition. ICP-MS analysis revealed a Fe/Co atomic ratio of ~0.15%, confirming minimal Fe adsorption on CoO_xH_y under conditions of limited mass transport via convection. At the beginning of the 5th cycle, mechanical stirring (500 rpm) was initiated and a large increase in OER current was observed in cycles 5-8 (Figure 1b). Subsequent cycles showed a decrease in

current when the stirring was turned off, and the OER activity was restored upon reinitiating the stirring again (Figure 1c,d). The full voltammetry curves of CoO_xH_y under various operation conditions are shown in Figure S2b,c.

The above results demonstrate the role of transport in Fe adsorption and subsequent OER activity. This phenomenon bears resemblance to other electrocatalytic reactions such oxygen reduction reaction (ORR) and CO_2 reduction reaction (CO_2RR), in which the reaction kinetics can be limited by the transport of reactants. Here, it is the delivery of the key catalytically active species that directly influences the reaction kinetics. In the case of the Co-Fe system, mechanical stirring facilitates the Fe transport by shortening the diffusion-layer thickness. Consequently, the higher density of soluble Fe species increases the probability of collision between Fe species and CoO_xH_y, thereby enabling more adsorption events.[35]

The effect of Fe incorporation was studied by chronoamperometry (CA) and cyclic voltammetry (CV). As shown in Figure S3, a Fe/Co ratio of ~4% was determined using ICP-MS after cycling 35 times from 0 to 0.7 V vs Hg/HgO with a scan rate 10 mV/s in Fe-spiked (0.1 ppm) KOH. This percentage is higher than that observed in the CA-spiked technique (~2.0% Fe relative to Co), hinting at some Fe integration in the subsurface of CoO_xH_y in CV mode. Notably, however, there was no evident peak shift in both CV and CA incorporated $CoFeO_xH_y$. This is evidence that Fe did not to substantial degree incorporate into the bulk $Co(OH)_2$ under either CV or CA mode because the Co redox wave is shifted positive in the mixed-metal compound, given findings from our previous research.[26, 36]

Apart from soluble-species transport, the applied potential also influences the Fe adsorption-desorption dynamics. The dissolution rate of FeOOH is dependent on the applied potential.[27, 37, 38] Considering the structural similarity between FeOOH and adsorbed Fe-$[O(H)]_x$ on CoO_xH_y, it is likely that the desorption of Fe-$[O(H)]_x$ is potential-controlled. The potential dependence may also be, in part, because the soluble Fe species in the electrolyte exist as charged ions such as $[Fe(OH)_4]^-$ and their movement and distribution within the double layer are affected by the applied potential.[38, 39] Isotope labelling could be further used to track the dynamic absorption and desorption processes of Fe.[23]

The effect of applied potential on Fe incorporation was studied by chronoamperometry (CA) measurements combined with ICP-MS analysis (Figure S4). Mechanical stirring (500 rpm) was used for all measurements. The quantity of Fe incorporated at potentials of 0.4 V and 0.65 V vs Hg/HgO was found to be similar, with a Fe/Co atomic ratio of ~1.8% (Figure S4a and b). At these potentials, Co can exist in different oxidation states, as indicated by the minor oxidation peak observed at ~0.65 V vs Hg/HgO (Figure S2a). A recent study showed that the electrochemical reaction occurring at the main oxidation peak (such as the peak at ~0.15 V vs Hg/HgO in this study) oxidized $Co(OH)_2$ into $CoO_2H_{1.5}\cdot 0.5H_2O$ with a nominal oxidation state of ~2.5.[40] Just prior to the onset of OER, $CoO_2H_{1.5}\cdot 0.5H_2O$ was further oxidized into CoOOH with a nominal oxidation state of ~3.3. The similar amount of Fe incorporation at these two potentials thus indicates that the number of Fe-accessible sites on CoO_xH_y is not significantly affected by the apparent structural transformation. However, when OER-relevant potentials were applied, the amount of incorporated Fe decreased with increasing positive potential (Figure 1f). In the CA-spiked $CoFeO_xH_y$ system, we analyzed the atomic ratio of Fe/Co by ICP-MS at different potentials during a constant electrolysis duration of 30 min. The Fe/Co atomic ratio decreased by ~0.008 h^{-1} at 0.7 V and 0.016 h^{-1} at 0.8 V vs Hg/HgO, consistent with higher Fe loss rate with increased applied potential associated with the Fe species being more soluble in higher-valent ferrate-like chemical states. This suggests that the incorporated Fe sites tend to desorb or dissolve during the OER process even in Fe-containing electrolyte. The loss of Fe in the OER region could be due to the further oxidation of Fe^{3+} species into high-valent FeO_4^{2-}, which is soluble in the electrolyte (but eventually decomposes spontaneously back to Fe^{3+} species).

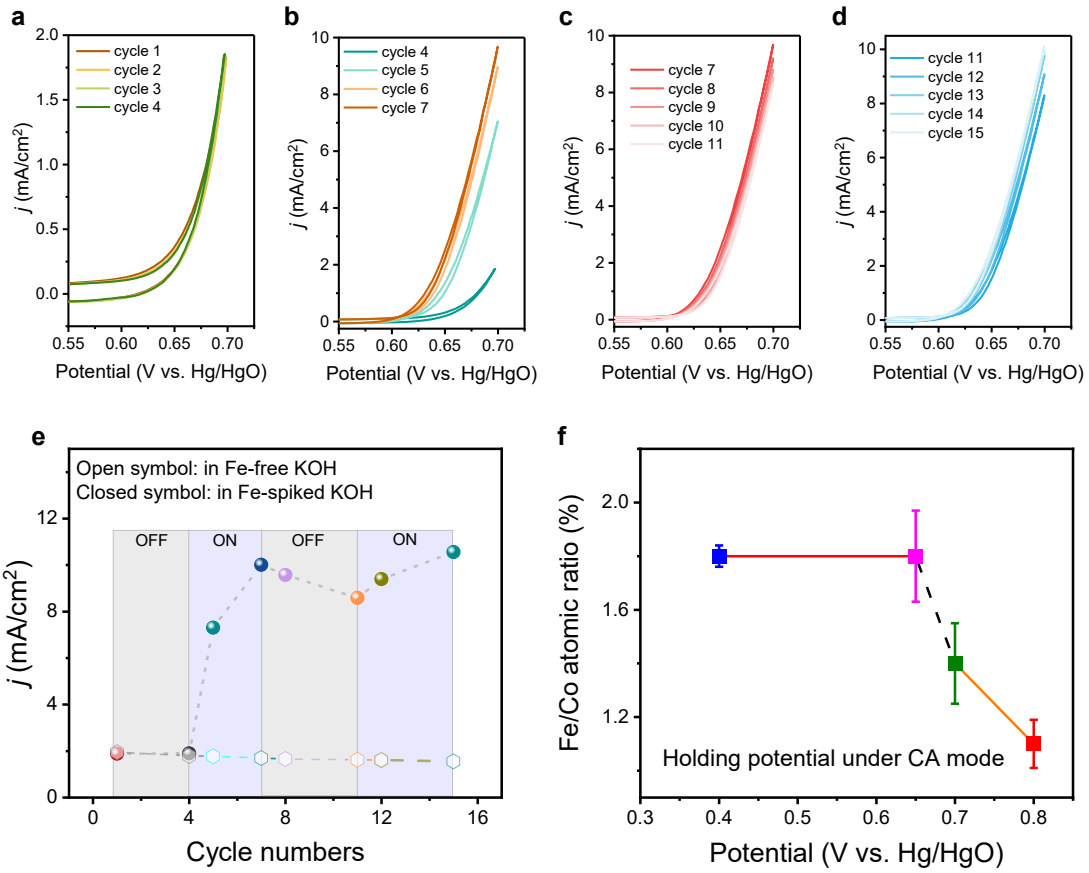

Figure 1. The effect of Fe-species transport and applied potential on the Fe adsorption on CoO_xH_y. (a-d) The OER current densities of CoO_xH_y film are affected by mechanical stirring of 1.0 M KOH electrolyte containing 0.1 ppm Fe^{3+}. Mechanical stirring was off at cycle 1-4 (a) and 8-11 (c). Mechanical stirring was on at cycle 5-7 (b) and 12-15 (d). (e) Summary of OER current densities of CoO_xH_y film collected at 0.7 V vs Hg/HgO (without *iR* correction) in Fe-free and Fe-containing (0.1 ppm) 1.0 M KOH with periodic stirring on and off. Hexagon symbols represent the activity tested in Fe-free electrolyte, while spheres are for samples in Fe-spiked KOH. (f) Effect of applied potential on the incorporated amount of Fe on CoO_xH_y. All samples were tested by holding corresponding potentials for 30 min to reach the maximum current density.

3.3 Effect of different Fe sites on OER catalysis

We next studied how the adsorbed Fe sites catalyze the OER and worked to obtain structural information about these sites during catalysis. Figure 2a shows the correlation between the OER current at an overpotential of 325 mV and the quantity of Fe within the catalyst film. Two types of $CoFeO_xH_y$ catalysts were prepared for comparison. The first type is CV-spiked $CoFeO_xH_y$ where

Fe sites predominantly reside on the surface of CoO_xH_y. The second type is a co-deposited film where the Fe atoms occupy all accessible sites including both bulk and surface sites. For the co-deposited film, a roughly linear relationship was observed (open blue squares in Figure 2a), with a slope of 0.23 ± 0.02 mA/nmol. A strong deviation from this linear relationship was observed for CV-spiked $CoFeO_xH_y$ (inset in Figure 2a). The surface-anchored Fe sites obtained by CV-spiking method appear to induce a positive "cooperative" effect on the OER catalysis kinetics.

To understand the intrinsic activity of different Fe sites, we calculated the turnover frequency (TOF) based on the total amount of Fe. Figure 2b shows the TOF_{Fe} at an overpotential of 325 mV as a function of Fe/Co atomic ratio. The CV curves corresponding to each data point are presented in Figure S5. Notably, the TOF_{Fe} of surface Fe sites (closed orange symbols) linearly increased with the Fe content, reaching a maximum TOF_{Fe} of 2.1 ± 0.3 s^{-1} at a Fe/Co atomic ratio of 4.0 ± 0.5%. This ascending trend of TOF_{Fe} suggests the existence of a cooperative effect among the surface Fe sites to promote the OER, which is consistent with the relationship between Fe content and OER current observed for CV-spiked $CoFeO_xH_y$, and our previous findings for the $NiFeO_xH_y$ system.[26] Adding more surface Fe species results in each Fe species having a higher apparent activity.

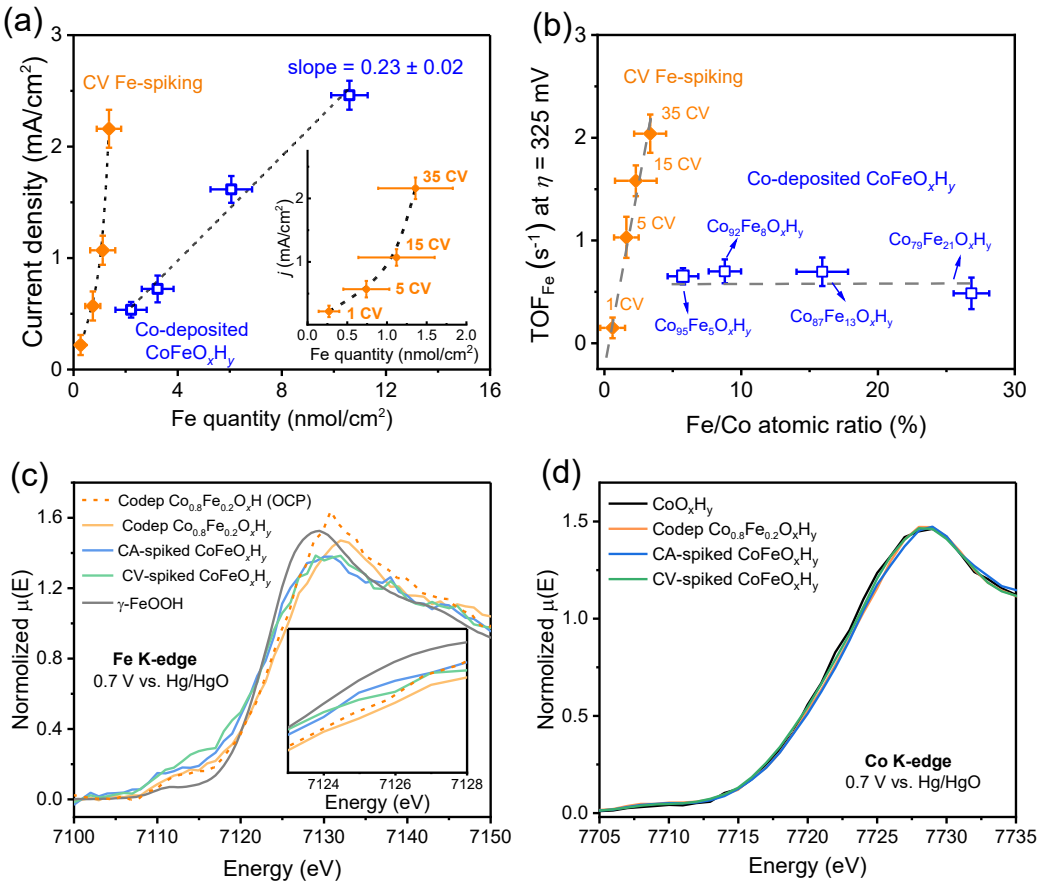

Figure 2. Intrinsic activity and structural information of Fe under various local environments on CoO_xH_y. (a) The OER current densities at an overpotential of 325 mV as a function of Fe quantity in CV-spiked $CoFeO_xH_y$ (closed orange symbols) and co-deposited $CoFeO_xH_y$ (open blue symbols). (b) Comparison of TOF_{Fe} of CV-spiked $CoFeO_xH_y$ and co-deposited $CoFeO_xH_y$ as a function of Fe/Co atomic ratio. The TOF_{Fe} data is based on taking Fe as the active sites and using the average of the forward and reverse sweep from CV curves at η = 325 mV. Metal contents and ratios were determined by ICP-MS. Error bars are based on samples measured in triplicate. (c,d) In-situ Fe K-edge (c) and Co K-edge (d) X-ray absorption near edge spectra (XANES) at a potential of 0.7 V vs. Hg/HgO for co-deposited $Co_{0.8}Fe_{0.2}O_xH_y$, CA-spiked $CoFeO_xH_y$ CV-spiked $CoFeO_xH_y$, and CoO_xH_y films. The ex-situ Fe K-edge spectra of γ-FeOOH and co-deposited $Co_{0.8}Fe_{0.2}O_xH_y$ at open circuit potential are presented for comparison. 1.0 M KOH containing 0.1 ppm Fe^{3+} was used as the electrolyte.

For comparison, the $TOF_{(Fe)}$ of co-deposited $CoFeO_xH_y$ was calculated. We accounted for all the Fe species in the co-deposited film, including both surface and bulk Fe species. As the co-deposited $CoFeO_xH_y$ is more active than the CoO_xH_y both before and after Fe absorption (on a total metal basis and ignoring the differences in Fe content between them), the Fe substituted into internal/non-surface Co sites may have non-negligible OER activity, although these internal Fe remain much less active than surface sites. Moreover, no cooperativity emerged with increasing Fe content for the co-deposited $CoFeO_xH_y$ series, as indicated by the much narrower distribution of TOF_{Fe} within a range of 0.4-0.7 s^{-1} (open blue symbols).

This lack of cooperative effect can be attributed to the uniform doping of Fe into the CoO_xH_y matrix where hypothesized cooperative Fe-Fe interactions are limited by intervening Co atoms. The higher TOF_{Fe} of surface Fe sites compared to that of the co-deposited film, which represents the average activity of surface and bulk Fe sites, thus supports the hypothesis that surface Fe sites are the highly active OER sites, especially when these surface absorbed Fe species are in high concentrations. We also note that the TOF_{Fe} of CV-spiked $CoFeO_xH_y$ at small Fe/Co ratio is lower than that of co-deposited $CoFeO_xH_y$. This could be attributed to the tendency of forming isolated Fe monomers when only trace Fe is incorporated, without cooperative effects of multiple Fe species interacting on the surface.[26]

To obtain insights into the local environment of $CoFeO_xH_y$ catalysts, *operando* X-ray absorption spectroscopy (XAS) was applied. The catalyst films were deposited on hydrophilic carbon papers with higher mass loading than on Pt/Ti substrate (see the Experimental Section) to enhance the XAS signal quality during data collection. Representative cyclic voltammetry of CoO_xH_y and $Co_{0.8}Fe_{0.2}O_xH_y$ films deposited on carbon-paper substrates for XAS data collection are shown in Figure S6. Freshly prepared CoO_xH_y films were first subjected to CV scans and CA electrolysis at 0.7 V vs Hg/HgO in Fe-spiked 1 M KOH electrolyte, enabling the incorporation of Fe species. Subsequently, XAS data was collected during constant potential steps. Co-deposited $Co_{0.8}Fe_{0.2}O_xH_y$ was prepared and measured for comparison to surface Fe-incorporated CoO_xH_y. The procedure for the XAS data collection is outlined in Figure S7.

Figure 2c shows the *in-situ* Fe K-edge X-ray absorption near-edge spectra (XANES) of different catalysts under OER conditions. The ex-situ spectrum of the γ-FeOOH standard along

with measurements at open circuit potential (OCP) were collected for comparison (Figure S8 and S9). Notably, the Fe K-edge energy positions of CV-spiked $CoFeO_xH_y$ and CA-spiked $CoFeO_xH_y$ are located ~1.0 eV negative than that of $Co_{0.8}Fe_{0.2}O_xH_y$ and more-resembled that of the γ-FeOOH standard. This proximity suggests a predominately +3 oxidation state for Fe in the CV and CA spiked $CoFeO_xH_y$ catalysts during OER catalysis, although certainly does not preclude minority higher-valence species from being active in the OER catalysis cycle. This is consistent with the preparation approach and electrochemical history affecting the local Fe coordination and apparent edge position to a greater degree, on average, than the application of electrochemical potential.[19, 27]

These XAS analyses illustrate a distinction between Fe species uniformly dispersed within the $Co_{0.8}Fe_{0.2}O_xH_y$ matrix and those incorporated from the Fe-containing electrolyte. The lower apparent degree of Fe oxidation (i.e. less-positive XAS edge) found in the CV- and CA-spiked $CoFeO_xH_y$, and its similarity to the γ-FeOOH standard, suggests that these added surface Fe-species are not intimately mixed with CoO_xH_y, as they are in the co-deposited material.

When a freshly prepared CoO_xH_y catalyst was immersed in KOH electrolyte without applied bias, the Co K-edge energy was consistent with the typical Co oxidation state of +2 (Figure 2d). Upon applying a potential of 0.7 V vs Hg/HgO, an oxidation to Co^{3+} was observed, as indicated by the positive shift in XAS edge. This suggests the transformation of initial hydroxides into oxyhydroxides under OER conditions, as expected. Similarly, the Co species in $Co_{0.8}Fe_{0.2}O_xH_y$, CA-spiked $CoFeO_xH_y$, and CV-spiked $CoFeO_xH_y$ exist as predominantly Co^{3+} under OER conditions (again not precluding minority nominal higher valence states). Although a difference in absorption energy was observed among these catalysts, it is not as significant as found in the Fe K-edge spectra. This is consistent with CoO_xH_y (or CoOOH during OER) acting in part as a support to accommodate different types of Fe species, while the latter plays a crucial role in catalyzing the OER.[16]

3.4 OER activity degradation and recovery

Stability is a significant factor affecting the applications of electrocatalysts. Chronoamperometry (CA) was used to investigate the stability of CV-spiking-prepared $CoFeO_xH_y$, which has the highest TOF_{Fe} when Fe is saturated on the catalyst surface. During the initial 4 h of CA test at an applied

potential of 0.75 V vs Hg/HgO, the OER current density decreased by about 50% even in Fe-containing electrolyte (Figure 3a). When an identical catalyst film was deposited on an electrochemical quartz crystal microbalance (EQCM) electrode, no loss in film mass was observed. Instead, the film mass increased slightly with the elongation of electrolysis duration. We also detected similar mass increase on a blank QCM upon immersion in the electrolyte (Figure S11), which may be due to changes in surface tension or wetting properties with exposure time.[38,39] We used ICP-MS to determine the cobalt content before and after electrolysis. No discernible mass loss was observed, indicating the stability of the catalyst film during OER. This is further evidenced by the SEM images (inset in Figure 3b), as the original nanosheet morphology was maintained after 4 h CA test. Moreover, the redox peaks corresponding to nominal Co^{2+}/Co^{3+} conversion display no noticeable change in terms of peak area and position after 4 h electrolysis, indicating that the number of redox active Co sites did not decrease (Figure 3b).

Considering the structural stability and electrochemical reversibility of the CoO_xH_y host, the origin of the activity degradation is likely due to the loss of Fe active sites. Indeed, ICP-MS analysis reveals that the Fe/Co atomic ratio decreased from 4.0 ± 0.5% to 2.0 ± 0.5% after 4 h electrolysis. This observation aligns with findings obtained through XPS analysis (Figure S12). The gradual depletion of surface Fe sites during the stability test further confirms the OER-triggered Fe desorption or oxidative dissolution.

Strategies to restore the surface Fe sites are thus expected to recover the OER activity. To this end, cyclic voltammetry was used at the end of the 4 h CA test. During this process, the OER activity recovered, approaching that observed before the CA test. Accompanying the activity increase is the rise of the Fe/Co ratio to 3.6 ± 0.5%. When the catalyst film underwent another round of CA test (stage 2 in Figure 3a), the newly recovered current again decreased.

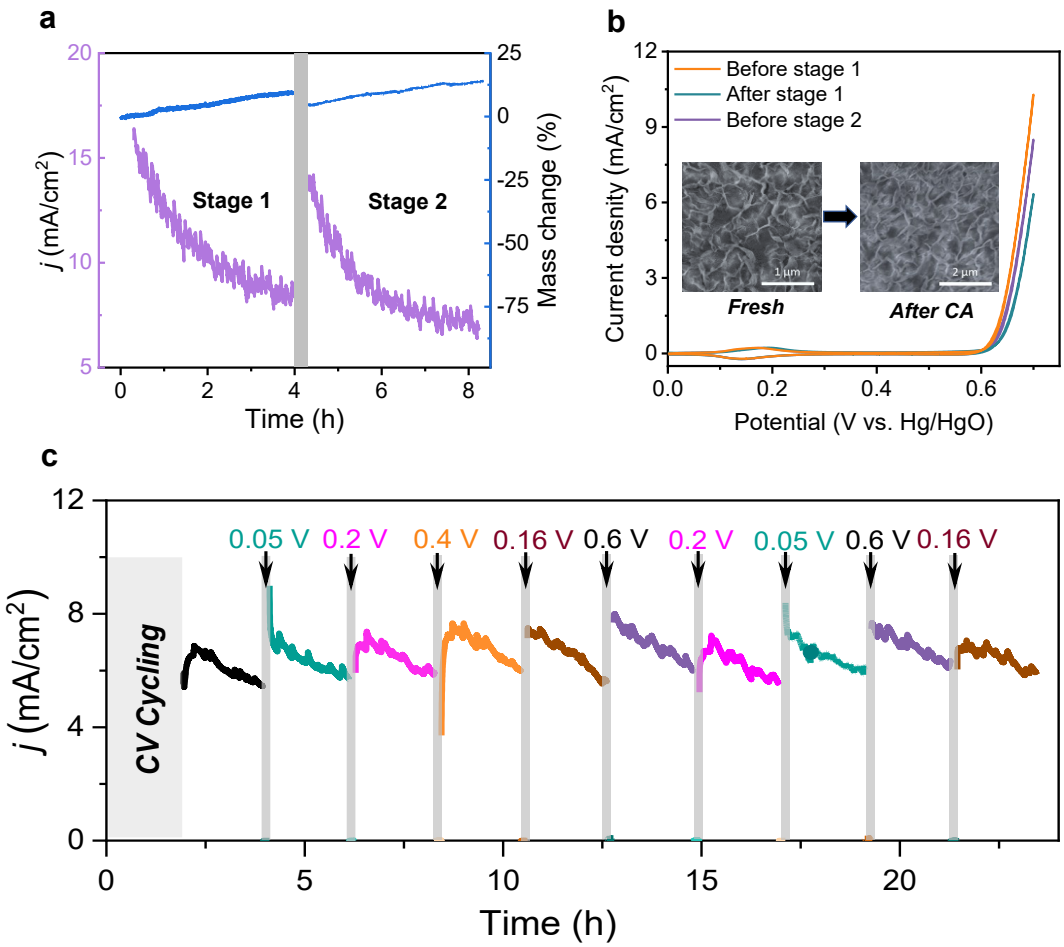

Figure 3. OER activity degradation and recovery of $CoFeO_xH_y$. (a) Mass change and alternate cyclic voltammetry and chronoamperometry test of CV-spiking-prepared $CoFeO_xH_y$ in 1.0 M KOH with 0.1 ppm Fe^{3+} added. 35 CV cycles were run before each CA test. A potential of 0.7 V vs. Hg/HgO was applied for the CA tests. (b) CV curves and SEM images (inset) of $CoFeO_xH_y$ before and after stage 1 CA test. (c) Alternative chronoamperometry test of $CoFeO_xH_y$ at applied potential of 0.7 V vs. Hg/HgO without *iR* correction in 0.1 ppm Fe-spiked KOH. Recovery potentials are 0.05 V, 0.16 V, 0.2 V, 0.4 V, 0.6 V vs. Hg/HgO with the duration of 10 min.

To gain a deeper understanding of whether the activity recovery is method or potential-dependent, 10 min of potential-controlled CA interruptions in a non-OER potential region were introduced between each 2 h CA electrolysis (held at 0.7 V vs Hg/HgO), as shown in Figure 3c. Potentials corresponding to Co^{2+} oxidation state (0.05 V), Co^{2+}/Co^{3+} transition region (0.16 V), Co^{3+} oxidation state (0.2 and 0.4 V), and the state just prior to OER onset (0.6 V) were selected

for investigation (Figure S13). Interestingly, regardless of the applied potential and the corresponding cobalt catalyst state, periodic activity recovery was consistently observed after applying the short-term CA interruptions. This suggests that the specific electrochemical history does not dominate the activity recovery. Instead, the critical factor appears to be the existence of a resting duration in the non-OER region. With sufficient time provided in the non-OER region, re-adsorption of Fe sites that had been previously desorbed from the catalyst surface during the continued electrolysis process appears to be occurring.

In contrast, the activity recovery of CoO_xH_y in Fe-free conditions was potential-dependent (Figure S14). Short-term CA interruptions holding CoO_xH_y in an oxidized state at 0.4 and 0.6 V failed to recover the OER current, while the lower applied potentials restored activity. This suggests that the activity loss is caused by structural change of CoO_xH_y during the OER process, such as further oxidation into a less-active phase, and activity can only be restored when the catalyst was reduced back to a lower oxidation state. Further supporting this hypothesis is the observation that the activity degradation of CoO_xH_y worsened with increasing OER overpotential (Figure S15a). When Fe was incorporated into the electrolyte, the extent of activity degradation became less pronounced (Figure S15b).

The ability of Fe to re-absorb under non-OER potentials upon depolarization of the anode below the OER potential regime could be used re-generate the OER activity when electrolysis is suspended because of fluctuation in demand or intermittency of renewable power supply, or as part of a programmed recovery period. The technoeconomic viability of this recovery approach depends on many factors and is beyond the scope of the current study. We also note that while our results are consistent with those of Chung et. al, who used isotopic labelled Fe to follow dissolution and re-deposition of Fe species,[24] the present work also addresses how mass transport affects the dissolution-redeposition process, how surface Fe sites exhibit cooperativity on CoO_xH_y like they do on NiO_xH_y, and how the operating potential affects the recovery of surface Fe-sites once lost which is useful in the design of advanced electrolyzers.

4 Conclusion

We studied the Fe adsorption-desorption dynamics at the interface between CoO_xH_y films and the electrolyte. The rate of Fe transport affected the Fe adsorption and thus the OER activity. Upon applying an OER-relevant potential, Fe desorption was found with increased potential. We delineated between two types of Fe active sites: "surface-localized" and "bulk/interior" Fe. The catalyst with surface Fe sites showed OER activity increasing super-linearly with the amount of adsorbed Fe (i.e. due to roughly linear TOF_{Fe} with the amount of Fe added) which suggests a cooperative effect among the surface Fe species on OER catalysis. In contrast, the co-deposited $CoFeO_xH_y$ demonstrated lower, yet consistent, activity per Fe site, as indicated by nearly constant TOF_{Fe} with amount of Fe species added. X-ray absorption spectroscopy (XAS) revealed the structural similarity between surface-adsorbed Fe sites and γ-FeOOH, providing structural insights into the OER-catalyzing Fe species. Finally, application of constant potential led to activity loss, which was caused by Fe desorption during continued electrolysis. The activity recovery depended on the application of a non-OER potential that promoted the soluble Fe re-adsorption. The Fe leaching also is consistent with the hypothesis that surface Fe are not strongly electronically interacting with most of the Co sites, as suggesting in previous work.[26]

Acknowledgement

This work was supported by the National Science Foundation Chemical Catalysis Program, Award #1955106 and #2400195. L.L. and Y.O. acknowledge support from the China Scholars Council. The ICP-MS instrument was funded by an NSF MRI Award #2117614. We acknowledge the use of shared instrumentation in the Center for Advanced Materials Characterization in Oregon (CAMCOR). L.L thanks Deen Sun (Chongqing University) and Lili Zhang (ISCE2) for the discussion.

Reference

(1) Walter, M. G.; Warren, E. L.; McKone, J. R.; Boettcher, S. W.; Mi, Q.; Santori, E. A.; Lewis, N. S. Solar Water Splitting Cells. *Chem. Rev.* **2010**, *110* (11), 6446-6473. DOI: 10.1021/cr1002326.

(2) Mckone, J. R.; Lewis, N. S.; Gray, H. B. Will Solar-Driven Water-Splitting Devices See the Light of Day? *Chem. Mater.* **2013**, *26*, 407-414.

(3) Pletcher, D.; Li, X. Prospects for alkaline zero gap water electrolysers for hydrogen production. *Int. J. Hydrogen Energy* **2011**, *36*, 15089-15104. DOI: 10.1016/j.ijhydene.2011.08.080.

(4) Armaroli, N.; Balzani, V. The future of energy supply: Challenges and opportunities. *Angew. Chem.* **2007**, *46* (1-2), 52-66. DOI: 10.1002/anie.200602373.

(5) Hunter, B. M.; Gray, H. B.; Muller, A. M. Earth-Abundant Heterogeneous Water Oxidation Catalysts. *Chem. Rev.* **2016**, *116* (22), 14120-14136. DOI: 10.1021/acs.chemrev.6b00398.
(6) Rossmeisl, J.; Qu, Z. W.; Zhu, H.; Kroes, G. J.; Nørskov, J. K. Electrolysis of water on oxide surfaces. *J. Electroanal. Chem.* **2007**, *607* (1), 83-89. DOI: https://doi.org/10.1016/j.jelechem.2006.11.008.
(7) Koper, M. T. M. Thermodynamic theory of multi-electron transfer reactions: Implications for electrocatalysis. *J. Electroanal. Chem.* **2011**, *660* (2), 254-260. DOI: 10.1016/j.jelechem.2010.10.004.
(8) Zeng, K.; Zhang, D. Recent progress in alkaline water electrolysis for hydrogen production and applications. *Prog. Energy Comb. Sci.* **2010**, *36* (3), 307-326. DOI: https://doi.org/10.1016/j.pecs.2009.11.002.
(9) Mills, T. J.; Lin, F.; Boettcher, S. W. Theory and simulations of electrocatalyst-coated semiconductor electrodes for solar water splitting. *Phys. Rev. Lett.* **2014**, *112* (14), 148304. DOI: 10.1103/PhysRevLett.112.148304.
(10) Liu, L.; Ou, Y.; Gao, D.; Yang, L.; Dong, H.; Xiao, P.; Zhang, Y. Surface engineering by a novel electrochemical activation method for the synthesis of Co^{3+} enriched $Co(OH)_2$/CoOOH heterostructure for water oxidation. *J. Power Sources* **2018**, *396*, 395-403. DOI: 10.1016/j.jpowsour.2018.06.030.
(11) Ou, Y.; Tian, W.; Liu, L.; Zhang, Y.; Xiao, P. Bimetallic $Co_2Mo_3O_8$ suboxides coupled with conductive cobalt nanowires for efficient and durable hydrogen evolution in alkaline electrolyte. *J. Mater. Chem. A* **2018**, *6* (12), 5217-5228. DOI: 10.1039/c7ta11401j.
(12) Liu, L. O., Yingqing; Deen Sun. Activity and stability of CoM_xO_y/Co_3O_4 (M=Mo, W, V) nano-arrays synthesized by self-templated method for water oxidization. *Chem. Eng. J.* **2021**. DOI: 10.1016/j.cej.2021.130063.
(13) Twight, L.; Tonsberg, A.; Samira, S.; Velinkar, K.; Dumpert, K.; Ou, Y.; Wang, L.; Nikolla, E.; Boettcher, S. W. Trace Fe activates perovskite nickelate OER catalysts in alkaline media via redox-active surface Ni species formed during electrocatalysis. *J. Catal.* **2024**, *432*, 115443. DOI: https://doi.org/10.1016/j.jcat.2024.115443.
(14) Gao, L.; Cui, X.; Sewell, C. D.; Li, J.; Lin, Z. Recent advances in activating surface reconstruction for the high-efficiency oxygen evolution reaction. *Chem. Soc. Rev.* **2021**, *50* (15), 8428-8469. DOI: 10.1039/d0cs00962h.
(15) Gao, L.; Cui, X.; Wang, Z.; Sewell, C. D.; Li, Z.; Liang, S.; Zhang, M.; Li, J.; Hu, Y.; Lin, Z. Operando unraveling photothermal-promoted dynamic active-sites generation in $NiFe_2O_4$ for markedly enhanced oxygen evolution. *Proc. Natl. Acad. Sci.* **2021**, *118* (7). DOI: 10.1073/pnas.2023421118.
(16) Burke, M. S.; Kast, M. G.; Trotochaud, L.; Smith, A. M.; Boettcher, S. W. Cobalt-Iron (Oxy)hydroxide Oxygen Evolution Electrocatalysts: The Role of Structure and Composition on Activity, Stability, and Mechanism. *J. Am. Chem. Soc.* **2015**, *137* (10), 3638-3648. DOI: 10.1021/jacs.5b00281.
(17) Stevens, M. B.; Enman, L. J.; Batchellor, A. S.; Cosby, M. R.; Vise, A. E.; Trang, C. D. M.; Boettcher, S. W. Measurement techniques for the study of thin film heterogeneous water oxidation electrocatalysts. *Chem. Mater.* **2017**, *29* (1), 120-140. DOI: 10.1021/acs.chemmater.6b02796.
(18) Friebel, D.; Louie, M. W.; Bajdich, M.; Sanwald, K. E.; Cai, Y.; Wise, A. M.; Cheng, M.-J.; Sokaras, D.; Weng, T.-C.; Alonso-Mori, R.; et al. Identification of Highly Active Fe Sites in (Ni,Fe)OOH for Electrocatalytic Water Splitting. *J. Am. Chem. Soc.* **2015**, *137* (3), 1305-1313. DOI: 10.1021/ja511559d.
(19) Enman, L. J.; Stevens, M. B.; Dahan, M. H.; Nellist, M. R.; Toroker, M. C.; Boettcher, S. W. Operando X-Ray Absorption Spectroscopy Shows Iron Oxidation Is Concurrent with Oxygen Evolution in Cobalt–Iron (Oxy)hydroxide Electrocatalysts. *Angew. Chem., Int. Ed.* **2018**, *57* (39), 12840-12844. DOI: doi:10.1002/anie.201808818.

(20) Chen, J. Y. C.; Dang, L.; Liang, H.; Bi, W.; Gerken, J. B.; Jin, S.; Alp, E. E.; Stahl, S. S. Operando Analysis of NiFe and Fe Oxyhydroxide Electrocatalysts for Water Oxidation: Detection of Fe^{4+} by Mössbauer Spectroscopy. *J. Am. Chem. Soc.* **2015**, *137* (48), 15090-15093. DOI: 10.1021/jacs.5b10699.
(21) Li, N.; Hadt, R. G.; Hayes, D.; Chen, L. X.; Nocera, D. G. Detection of high-valent iron species in alloyed oxidic cobaltates for catalysing the oxygen evolution reaction. *Nat. Commun.* **2021**, *12* (1), 4218. DOI: 10.1038/s41467-021-24453-6.
(22) Fabbri, E.; Schmidt, T. J. Oxygen Evolution Reaction—The Enigma in Water Electrolysis. *ACS Catal.* **2018**, *8* (10), 9765-9774. DOI: 10.1021/acscatal.8b02712.
(23) Binninger, T.; Mohamed, R.; Waltar, K.; Fabbri, E.; Levecque, P.; Kötz, R.; Schmidt, T. J. Thermodynamic explanation of the universal correlation between oxygen evolution activity and corrosion of oxide catalysts. *Scientific Reports* **2015**, *5*, 12167. DOI: 10.1038/srep12167.
(24) Chung, D. Y.; Lopes, P. P.; Farinazzo Bergamo Dias Martins, P.; He, H.; Kawaguchi, T.; Zapol, P.; You, H.; Tripkovic, D.; Strmcnik, D.; Zhu, Y.; et al. Dynamic stability of active sites in hydr(oxy)oxides for the oxygen evolution reaction. *Nat. Energy* **2020**, *5* (3), 222-230. DOI: 10.1038/s41560-020-0576-y.
(25) Kuai, C.; Xu, Z.; Xi, C.; Hu, A.; Yang, Z.; Zhang, Y.; Sun, C.-J.; Li, L.; Sokaras, D.; Dong, C.; et al. Phase segregation reversibility in mixed-metal hydroxide water oxidation catalysts. *Nat. Catal.* **2020**, *3* (9), 743-753. DOI: 10.1038/s41929-020-0496-z.
(26) Ou, Y.; Twight, L. P.; Samanta, B.; Liu, L.; Biswas, S.; Fehrs, J. L.; Sagui, N. A.; Villalobos, J.; Morales-Santelices, J.; Antipin, D.; et al. Cooperative Fe sites on transition metal (oxy)hydroxides drive high oxygen evolution activity in base. *Nat. Commun.* **2023**, *14* (1), 7688. DOI: 10.1038/s41467-023-43305-z.
(27) Zhang, T.; Nellist, M.; Enman, L.; Xiang, J.; Boettcher, S. Modes of Fe incorporation in Co-Fe (oxy)hydroxide oxygen evolution electrocatalysts. *ChemSusChem* **2018**, *12* (9), 2015-2021. DOI: doi:10.1002/cssc.201801975.
(28) Enman, L. J.; Vise, A. E.; Burke Stevens, M.; Boettcher, S. W. Effects of Metal Electrode Support on the Catalytic Activity of Fe(oxy)hydroxide for the Oxygen Evolution Reaction in Alkaline Media. *ChemPhysChem* **2019**, *20* (22), 3089-3095. DOI: https://doi.org/10.1002/cphc.201900511.
(29) Liu, L.; Twight, L. P.; Fehrs, J. L.; Ou, Y.; Sun, D.; Boettcher, S. W. Purification of Residual Ni and Co Hydroxides from Fe-Free Alkaline Electrolyte for Electrocatalysis Studies. *ChemElectroChem* **2022**, *9* (15), e202200279. DOI: https://doi.org/10.1002/celc.202200279.
(30) Noorbakhsh, A.; Mirkalaei, M. M.; Yousefi, M. H.; Manochehri, S. Electrodeposition of Cobalt Oxide Nanostructure on the Glassy Carbon Electrode for Electrocatalytic Determination of para-Nitrophenol. *Electroanalysis* **2014**, *26* (12), 2716-2726. DOI: 10.1002/elan.201400386.
(31) Koza, J. A.; Hull, C. M.; Liu, Y.-C.; Switzer, J. A. Deposition of β-$Co(OH)_2$ Films by Electrochemical Reduction of Tris(ethylenediamine)cobalt(III) in Alkaline Solution. *Chem. Mater.* **2013**, *25* (9), 1922-1926. DOI: 10.1021/cm400579k.
(32) Smith, R. D.; Prevot, M. S.; Fagan, R. D.; Trudel, S.; Berlinguette, C. P. Water oxidation catalysis: electrocatalytic response to metal stoichiometry in amorphous metal oxide films containing iron, cobalt, and nickel. *J. Am. Chem. Soc.* **2013**, *135* (31), 11580-11586. DOI: 10.1021/ja403102j.
(33) Corrigan, D. A.; Bendert, R. M. Effect of Coprecipitated Metal Ions on the Electrochemistry of Nickel Hydroxide Thin Films: Cyclic Voltammetry in 1M KOH. *J. Electrochem. Soc.* **1989**, *136*, 723-728. DOI: 10.1149/1.2096717.
(34) Trotochaud, L.; Young, S. L.; Ranney, J. K.; Boettcher, S. W. Nickel-iron oxyhydroxide oxygen-evolution electrocatalysts: the role of intentional and incidental iron incorporation. *J. Am. Chem. Soc.* **2014**, *136* (18), 6744-6753. DOI: 10.1021/ja502379c.
(35) Thorarinsdottir, A. E.; Erdosy, D. P.; Costentin, C.; Mason, J. A.; Nocera, D. G. Enhanced activity for the oxygen reduction reaction in microporous water. *Nat. Catal.* **2023**, *6* (5), 425-434. DOI: 10.1038/s41929-023-00958-9.

(36) Stevens, M. B.; Trang, C. D. M.; Enman, L. J.; Deng, J.; Boettcher, S. W. Reactive Fe-Sites in Ni/Fe (oxy)hydroxide are responsible for exceptional oxygen electrocatalysis activity. *J. Am. Chem. Soc.* **2017**, *139* (33), 11361-11364. DOI: 10.1021/jacs.7b07117.
(37) Hunter, B. M.; Thompson, N. B.; Müller, A. M.; Rossman, G. R.; Hill, M. G.; Winkler, J. R.; Gray, H. B. Trapping an Iron(VI) Water-Splitting Intermediate in Nonaqueous Media. *Joule* **2018**, *2* (4), 747-763. DOI: 10.1016/j.joule.2018.01.008.
(38) Zou, S.; Burke, M. S.; Kast, M. G.; Fan, J.; Danilovic, N.; Boettcher, S. W. Fe (Oxy)hydroxide Oxygen Evolution Reaction Electrocatalysis: Intrinsic Activity and the Roles of Electrical Conductivity, Substrate, and Dissolution. *Chem. Mater.* **2015**, *27* (23), 8011-8020. DOI: 10.1021/acs.chemmater.5b03404.
(39) Feng, C.; Faheem, M. B.; Fu, J.; Xiao, Y.; Li, C.; Li, Y. Fe-Based Electrocatalysts for Oxygen Evolution Reaction: Progress and Perspectives. *ACS Catal.* **2020**, *10* (7), 4019-4047. DOI: 10.1021/acscatal.9b05445.
(40) Mefford, J. T.; Akbashev, A. R.; Kang, M.; Bentley, C. L.; Gent, W. E.; Deng, H. D.; Alsem, D. H.; Yu, Y.-S.; Salmon, N. J.; Shapiro, D. A.; et al. Correlative operando microscopy of oxygen evolution electrocatalysts. *Nature* **2021**, *593* (7857), 67-73. DOI: 10.1038/s41586-021-03454-x.